Check for updates

An integrated experimental and theoretical approach to probe Cr(VI) uptake using decorated halloysite nanotubes for efficient water treatment†

Syed Nadeem Ahmad Shah, [ID] [a] Sonia Zulfiqar, [ID] *[bc] Fernando Ruipérez, [d] Muhammad Rafique, [e] Mudassir Iqbal, [ID] [a] Michael J. Forrester, [ID] [c] Muhammad Ilyas Sarwar (Late)[e] and Eric W. Cochran*[c]

Halloysite nanotubes (HNTs) were surface functionalized using four distinct chemical moieties (amidoxime, hydrazone, ethylenediamine (EDA), and diethylenetriamine (DETA)), producing modified HNTs (H1–H4) capable of binding with Cr(VI) ions. Advanced techniques like FTIR, XRD, SEM, and EDX provided evidence of the successful functionalization of these HNTs. Notably, the functionalization occurred on the surface of HNTs, rather than within the interlayer or lumen. These decorated HNTs were effective in capturing Cr(VI) ions at optimized sorption parameters, with adsorption rates ranging between 58–94%, as confirmed by atomic absorption spectroscopy (AAS). The mechanism of adsorption was further scrutinized through the Freundlich and Langmuir isotherms. Langmuir isotherms revealed the nearest fit to the data suggesting the monolayer adsorption of Cr(VI) ions onto the nanotubes, indicating a favorable adsorption process. It was hypothesized that Cr(VI) ions are primarily attracted to the amine groups on the modified nanotubes. Quantum chemical calculations further revealed that HNTs functionalized with hydrazone structures (H2) demonstrated a higher affinity (interaction energy -26.33 kcal mol^{-1}) for the Cr(VI) ions. This can be explained by the formation of stronger hydrogen bonds with the NH moieties of the hydrazone moiety, than those established by the OH of oxime (H1) and longer amine chains (H3 and H4), respectively. Overall, the findings suggest that these decorated HNTs could serve as an effective and cost-efficient solution for treating water pollution.

1. Introduction

The rapid growth of industries has raised serious concerns about water scarcity and pollution.[1] One of the primary sources of water pollution comes from dyes, heavy metals and organic pollutants. The removal of heavy metals, which are not biodegradable, from wastewater is especially important.[2,3] As industries such as steel production, electroplating, battery manufacturing, tanneries, and petroleum refining expand, they release increasing amounts of heavy metals into water bodies, either directly or indirectly.[4–6] Typical heavy metals found in wastewater include copper, cadmium, chromium, mercury,

[a]Department of Chemistry, School of Natural Sciences, National University of Sciences and Technology, H-12, Islamabad, 44000, Pakistan

[b]Department of Chemistry, Faculty of Science, University of Ostrava, 30. Dubna 22, Ostrava 701 03, Czech Republic. E-mail: sonia.zulfiqar@osu.cz; zulfiqar@iastate.edu

[c]Department of Chemical and Biological Engineering, Iowa State University, Sweeney Hall, 618 Bissell Road, Ames, Iowa 50011, USA. E-mail: ecochran@iastate.edu

[d]POLYMAT, Physical Chemistry Department, Faculty of Pharmacy, University of the Basque Country UPV/EHU, 01006 Vitoria-Gasteiz, Spain

[e]Department of Chemistry, Quaid-i-Azam University, Islamabad, 45320, Pakistan

† Electronic supplementary information (ESI) available. See DOI: https://doi.org/10.1039/d3ra07675j

zinc, and nickel.[7,8] Notably, chromium exist in two forms; Cr(VI) and Cr(III). However, Cr(VI) ions are 500 times more toxic than Cr(III).[9] As a result, Cr(VI) is one of the most harmful pollutants. These ions are discharged from various industries, including tanneries, textiles, photography, battery production, and others.[10] Due to their non-biodegradable nature, they enter the food chain and can cause health issues ranging from skin cancer to kidney and liver damage.[11–15] In some cases, the concentration of Cr(VI) ions in industrial wastewater can be extremely high, with levels in tannery waste even reaching up to 2500 mg L^{-1} in extreme situations.[16,17]

A variety of techniques have been documented for extracting Cr(VI) ions. These techniques encompass methods such as ion exchange, precipitation, reverse osmosis, electrochemical treatment, and adsorption.[18–23] These approaches primarily focus on transforming the more hazardous Cr(VI) ions into the less harmful Cr(III) ions. However, each method comes with its own set of drawbacks. For instance, the precipitation process can lead to sludge accumulation. The ion exchange method might require expensive reagents, advanced setups, and can potentially produce undesirable by-products. Electrochemical treatments can also be costly. Among these techniques, adsorption is often viewed as a more cost-effective and

economically sound alternative for the uptake of Cr(VI) ions. The success of this method largely depends on the choice of the adsorbent used. The efficacy of Cr(VI) ion removal centers on selecting the right adsorbent. Commonly used adsorbents include activated carbon, alumina, silica, nano-metal oxides, and carbon nanotubes (CNTs).[24–38] These materials have demonstrated decent efficiency in adsorption, however, a major drawback is their high cost and the complex processes required to remove them from wastewater post-adsorption.

In light of these challenges, clay materials have emerged as particularly effective adsorbents for removing heavy metals from wastewater.[39] This preference for clay materials can be attributed to several of their inherent qualities. They naturally form stacks, have a large specific surface area, are widely available, and are non-toxic. Furthermore, they are cost-effective. Despite these advantages, it is worth noting that the adsorption capacity of clays for Cr(VI) ions remains somewhat limited. This limitation is partly because certain sites within their structure remain inaccessible. Yet, this efficiency can be significantly boosted by applying surface functionalization to the adsorbents.[40–45] Many sponges and synthetic materials like polyurethane and HNTs-polyurethane nanocomposites have been reported.[46] Likewise; various organic, inorganic adsorption materials and their hybrids, hollow spheres, hollow microtubes, magnetic CNTs and nanocomposites have been fabricated for wastewater treatment.[47–51] Among them, some have greater adsorption capacity for cationic and anionic dyes, while others have a high adsorption capacity for heavy metal ions. These adsorbents also contain graphene and carbon nanotubes (CNTs) which show enhanced adsorption efficiency, however, their toxicity and non-biodegradability limit their applications in water treatment.[52]

Recently, Halloysite Nanotubes (HNTs) have gained importance as superior adsorbents in the realm of wastewater treatment. Their rise to prominence can be attributed to a myriad of distinctive features. These include higher surface area and an impressive length-to-diameter ratio. Additionally, HNTs are celebrated for their biocompatible "green" chemistry, which emphasizes environment-friendly practices. A notable characteristic of HNTs is the substantial presence of hydroxyl groups in their composition.[53–60] However, when it comes to the removal of chromium(VI) ions, unmodified HNTs demonstrate a somewhat limited sorption capacity. Despite this limitation, it has been observed that the adsorption efficiency can witness a remarkable boost when the surface of the HNTs is modified with specific functional groups. This modification enhances the uptake of Cr(VI) ions.[61–68] As adsorbents, HNTs have been studied in the removal of Cr(VI)[69] and water treatment.[70,71] For instance, Kai *et al.* reported that the modified HNTs (HNTs-PUS) displayed greater adsorption capacity of 77.4% for the removal of Cr(VI).[69] Shin-ichi *et al.* investigated the effect of halloysite nanotubes functionalized with poly(amidoamine) dendrimers on Cr(VI) uptake and they found increased adsorption performance.[72] Such studies disclosed that HNTs showed higher adsorption capacity for Cr(VI) removal when they underwent surface modification. Hence, it is crucial to design new and facile methods to functionalize HNTs in order to boost adsorption capabilities. Among the functional

groups, amino groups stand out as particularly effective for the removal of Cr(VI) ions. Their efficacy is rooted in their ability to extract metal ions, facilitated by processes of chelation and electrostatic interaction.

Herein, we introduced a novel approach where we synthesized new adsorbents by functionalizing the external surface of Halloysite nanotubes (HNTs). This modification involved integrating various functional groups, such as amidoxime, hydrazone, ethylenediamine (EDA), and diethylenetriamine (DETA). To the best of our knowledge, this is the first time these specific modifications have been implemented on HNTs. To verify and explore the properties of these modified nanotubes, they underwent characterization using a suite of advanced techniques. Fourier Transform Infrared Spectroscopy (FTIR), X-ray diffraction (XRD), Scanning Electron Microscopy (SEM), and Energy Dispersive X-ray Spectroscopy (EDX) were employed for this purpose. Following this, the modified HNTs (H1–H4), were tested for their efficacy in removing Cr(VI) ions from the aqueous solutions. A series of batch experiments were conducted to ascertain their performance. These experiments were designed to operate under optimized conditions, factoring in specific parameters such as the duration of contact, pH level, and the concentration of the adsorbate present. For a deeper understanding of the adsorption dynamics and underlying mechanisms, well-established Freundlich and Langmuir models were used. One of the standout revelations from our quantum chemical calculations was the superior performance of HNTs that had been functionalized with hydrazone structures (H2). These specific HNTs showcased a remarkably higher affinity for Cr(VI) ions, possessing an interaction energy of -26.33 kcal mol^{-1}. The reason behind this increased affinity can be attributed to the formation of robust hydrogen bonds, particularly those involving the NH components of the hydrazone group. Interestingly, these bonds were found to be stronger than those created by the OH components of oxime (H1) and the elongated amine chains in H3 and H4 samples. These modified HNTs not only offer promising potential for effectively removing the Cr(VI) ions but also present an economical alternative, making them highly suitable for wastewater treatment applications.

2. Experimental

2.1. Materials

Halloysite nanotubes (HNTs) with the chemical formula $Al_2Si_2O_5(OH)_4 \cdot 2H_2O$ and hydroxylamine (50 wt% in H_2O) were procured from Sigma-Aldrich. Other chemicals such as 4-nitrophthalonitrile, potassium carbonate, hydrazine, ethylenediamine (EDA), diethylenetriamine (DETA), dry toluene, ethanol, *N*-methylpyrrolidone (NMP), tetrahydrofuran (THF), and potassium chromate were of analytical grade. These reagents were utilized as received, without undergoing any further purification.

2.2. Preparation of functionalized halloysite nanotubes (f-HNTs)

2.2.1 Nitrile-functionalized HNTs.
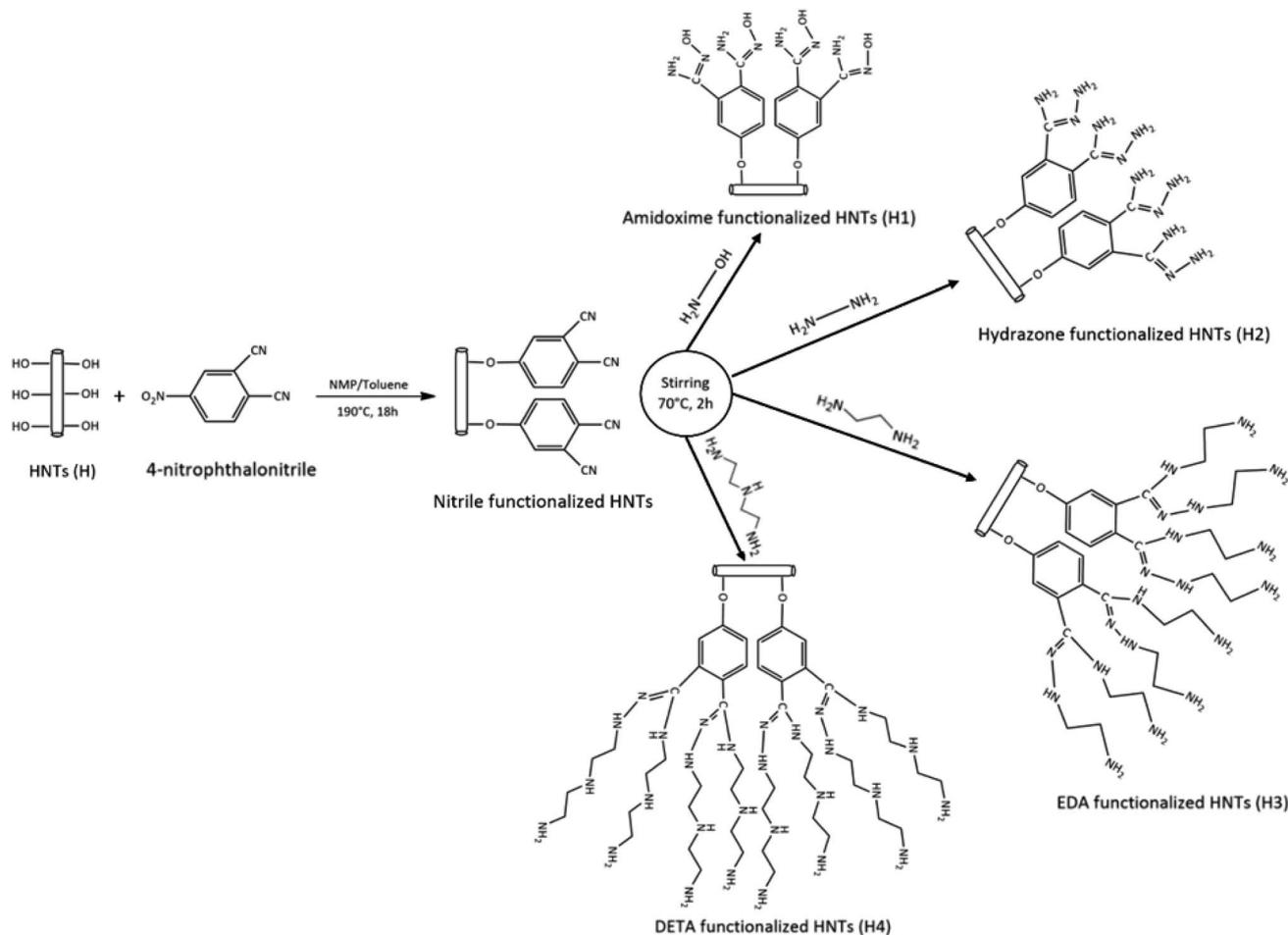To modify the surface of halloysite nanotubes (H), the reaction was performed in an inert

Fig. 1 Schematic illustration for the formation of functionalized HNTs.

atmosphere. This was done using a 250 mL three-neck round bottom flask, equipped with a magnetic stirrer, Dean Stark trap, condenser, and a nitrogen inlet. To ensure a dry environment, a calcium chloride drying tube was affixed atop the condenser. The procedure began by injecting NMP (50 mL) into the reaction flask with a syringe. Following that, HNTs (7 g) and potassium carbonate (5.53 g) were introduced and continuously stirred. Additionally, dry toluene (10 mL) was incorporated as an azeotropic agent. The reaction mixture was then heated to 140 °C and maintained for 3 hours, ensuring the complete elimination of azeotropic water. After this, the temperature was increased to 190 °C. At this point, 4-nitrophthalonitrile (4.7 g, 27 mmol) was added to the flask. The reaction mixture underwent reflux for a duration of 18 hours. Once completed, the flask's contents were cooled. The resultant dark brownish-black product was then diluted using THF (50 mL) and was thoroughly washed several times with THF and a methanol/water mixture (80/20 ratio), filtered, and subsequently dried in a vacuum oven at 80 °C overnight; Yield 88%; Coverage Index 3.1 mmol g^{-1}.[73] The product is referred to as the nitrile-functionalized HNTs, which serve as an intermediate to prepare f-HNTs (H1–H4). This product was then subjected to interactions with various chemical reagents to introduce different functionalities onto the

halloysite nanotubes, as illustrated in Fig. 1. Throughout the process, the reactions were periodically monitored using TLC to confirm their progress and completion.

2.2.2 Amidoxime-functionalized HNTs (H1). The process of creating H1 starts by dissolving 2 g of nitrile-functionalized HNTs in ethanol. Following this, a hydroxylamine solution (0.15 mL) was introduced while continuously stirring at 70 °C for a duration of 3 hours. As time progressed, there was a formation of dark brown precipitates. These precipitates were subsequently isolated using centrifugation, rinsed with ethanol, and dried in a vacuum oven as depicted in Fig. 1.

2.2.3 Hydrazone-functionalized HNTs (H2). On the other hand, to produce H2, 2 g of nitrile-functionalized HNTs were first dissolved in ethanol. Then, hydrazine solution (0.17 mL) was added. This mixture was agitated for 3 hours at 70 °C. As the chemical reaction took place, the solution underwent a color change, becoming darker, leading to the emergence of dark brown precipitates. These precipitates were separated using centrifugation, washed with ethanol, and subsequently dried under a vacuum (Fig. 1).

2.2.4 EDA-functionalized HNTs (H3). To synthesize H3, 2 g of nitrile-functionalized HNTs were dispersed in ethanol within a round-bottom flask. Subsequently, 0.35 mL of

ethylenediamine was added while maintaining continuous stirring at a temperature of 70 °C over a span of 3 hours. As the reaction proceeded, dark brown precipitates emerged. These were then separated using centrifugation (Fig. 1). After separation, the precipitates were rinsed with ethanol and left to dry in a vacuum oven overnight.

2.2.5 DETA-functionalized HNTs (H4). Similarly, for the production of H4, 2 g of nitrile-functionalized HNTs were dissolved in ethanol in a round-bottom flask. This was followed by adding 0.56 mL of diethylenetriamine and maintaining a continuous stirring for 3 hours at 70 °C. The resulting precipitates were then isolated, washed with ethanol, and dried overnight in a vacuum oven at 60 °C (Fig. 1).

2.3. Adsorption of chromium(VI) ions

The effectiveness of the functionalized HNTs was evaluated by using them for the extraction of Cr(VI) ions. Factors such as pH, contact time, and the concentration of the metal ions have a direct impact on the adsorption capabilities of all the f-HNTs. As a result, a series of batch experiments were conducted to fine-tune these factors and achieve optimal adsorption. 10 mL of solutions containing various initial concentrations of Cr(VI) ions, ranging from 10 to 150 ppm were measured into conical flasks, and 10 mg of f-HNTs, acting as the adsorbent, were introduced.[65–68] Subsequently, these samples were stirred at a speed of 180 rpm using a mechanical shaker, maintained at room temperature. Both the Freundlich and Langmuir adsorption models were employed to assess the suitability of the adsorption process. Once equilibrium was reached, the adsorbent underwent centrifugation at a speed of 3500 rpm for a duration of 10 minutes and was then filtered. The residual concentration of Cr(VI) ions post-adsorption was measured using atomic absorption spectroscopy. The equilibrium adsorption capacity of the Cr(VI) ions was ascertained using the following equation:

$$\% \text{ removal} = \frac{C_o - C_e}{C_o} \times 100$$

where C_o and C_e are the initial and equilibrium concentrations of Cr(VI) ions.

2.4. Computational details

All calculations based on density functional theory (DFT) were executed using the Gaussian 16 suite of programs.[74] For geometry optimizations, the long-range corrected ωB97XD functional was used,[75] which also incorporates dispersion corrections, together with the 6-31+G(d,p) double-zeta basis set including diffuse and polarization functions. This type of basis set provides a good compromise between computational cost and accuracy.[76] Harmonic vibrational frequencies were subsequently derived at the same level of theory, using analytical differentiation of the gradients to ascertain if the identified structures were either minima or transition states. Notably, all the structures demonstrated real frequencies across all their normal vibrational modes. These identified frequencies were subsequently utilized to evaluate the zero-point vibrational

energy (ZPVE) in the harmonic oscillator approximation. To further refine the electronic energy, single-point calculations were conducted using the 6-311++G(2df,2p) triple-zeta basis set, including diffuse and polarization functions as well. This large basis set is particularly suitable for calculating molecular properties and interaction energies.[77] The energy required to bind $HCrO_4^-$ to the models of functionalized halloysite nanotubes was estimated as follows:

$$\Delta E_{CP} = E_0 \text{ (complex)} - E_0 (H_i) - E_0 (HCrO_4^-)$$

E_0 represents the electronic energy, along with the zero-point energy correction, of the complexes of halloysite (H_i, $i = 1$–4) with $HCrO_4^-$ and the individual molecules. The term ΔE_{CP} signifies the binding energy, including the correction of the basis set superposition error (BSSE) by means of the counterpoise method.[78,79]

2.5. Characterization

The IR spectra of the produced materials were captured using a Bruker Tensor II FTIR spectrometer, ranging from 400 to 4000 cm^{-1}, to identify the functional groups within the f-HNTs. To ascertain the crystallinity and phase of both pure and f-HNTs, X-ray diffraction patterns were carefully analyzed using a Rigaku diffractometer, which operated with an incident wavelength of Cu Kα ($\lambda = 1.542$ Å). To assess the morphology and microstructures of both unmodified and f-HNTs, scanning electron microscopy (SEM, MIRA3 TESCAN) was employed at an operating voltage of 10 kV. In addition, energy-dispersive X-ray spectroscopy (EDX), integrated with SEM, was utilized for the elemental analysis of the nanomaterials. Furthermore, a Shimadzu AA 670 flame atomic absorption spectrophotometer was used specifically to measure the chromium(VI) ions.

3. Results and discussion

Several varieties of f-HNTs were synthesized using distinct reagents, with the aim of introducing specific functional groups that can interact with Cr(VI) ions. These nanomaterials showcased their potential as effective adsorbents, featuring donor sites on their surfaces. The characteristics of these f-HNTs were confirmed using a range of analytical techniques. The adsorption capacity for metal ions was meticulously examined using AAS under optimal conditions. In addition, adsorption experiments were conducted, and the resulting data was subsequently interpreted using both Freundlich and Langmuir models.

3.1. Structure elucidation

The structure of the f-HNTs was elucidated using the FTIR spectroscopy. Absorption bands observed at 3688 and 3619 cm^{-1} correspond to the vibrations of the inner surface O–H groups of aluminol (Al–OH). The bending vibrational band of aluminol groups (Al–OH) appeared at 910 cm^{-1}. The characteristic band at 3648 cm^{-1} could be due to the absorbed water. A notable band at 1001 cm^{-1} indicated the presence of Si–O–Si on the HNTs' outer surface. Several bands remained
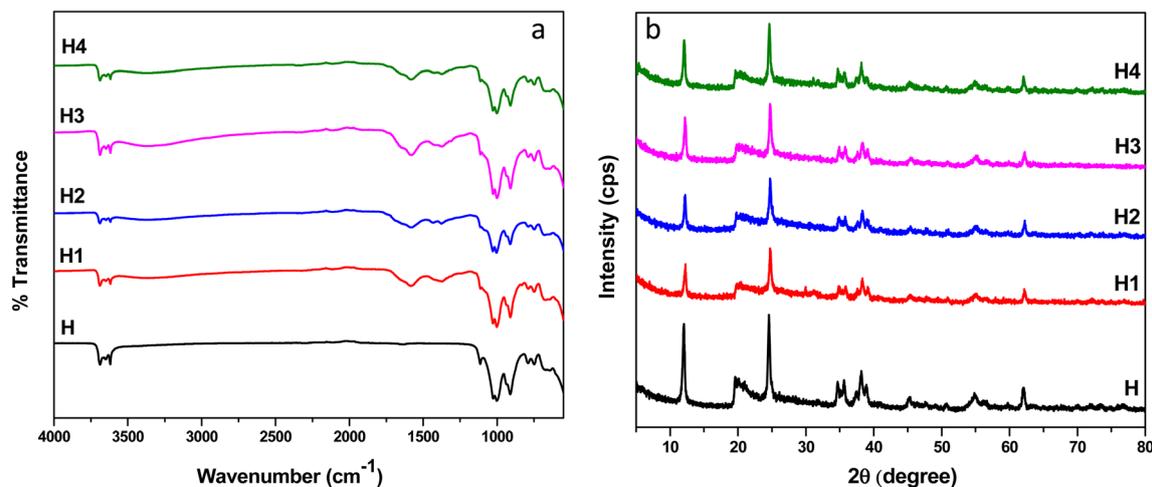
Fig. 2 (a) FTIR spectra and (b) XRD patterns of pristine HNTs (H) and f-HNTs (H1–H4) samples.

unchanged post-functionalization, suggesting that the fundamental structure of HNTs remained intact. However, post-functionalization also introduced some new bands owing to various functionalities introduced on the surface of HNTs, as visualized in Fig. 2a. The C=N and aromatic C=C stretching vibration was observed at 1582 cm^{-1}, and a distinct C–N stretch was identified at 1373 cm^{-1}, affirming the successful modification of HNTs. Bands representing N–H stretching vibrations were seen in the 3360–3370 cm^{-1} range. These findings underscored the successful functionalization of HNTs' surface with four distinct groups, referred to as H1, H2, H3, and H4 respectively.

The structure of pristine and functionalized HNTs was further verified by using X-ray diffraction analysis. The diffractograms for both pristine and f-HNTs are illustrated in Fig. 2b. These characteristic peak positions for pristine HNTs (H) appeared at 12.13°, 20.01°, 24.59°, 35.01°, 38.37°, 54.91° and 62.17° according to the standard JCPDS card no. 29-1487.[80] Relative to the pristine HNTs (H), the positions of the diffraction peaks for the four functionalized HNTs profiles (H1–H4) remain largely consistent, indicating that the crystalline structure of the HNTs remains intact post-surface functionalization, with no discernible shift in the diffraction peaks. Nonetheless, there is a noticeable reduction in the intensity of the diffraction peaks in the H1–H4 samples compared to H, suggesting that the outer surface of the halloysite nanotubes underwent successful modification. XRD patterns further validate the absence of HNTs intercalation during the functionalization step.

3.2. Morphology and elemental analysis

The surface morphology of pristine HNTs (H) and modified HNTs (H1–H4) was examined using a scanning electron microscope (SEM). The unique surface chemistry of halloysite nanotubes (HNTs) enables the adjustment of their physicochemical characteristics by manipulating the chemistry of their constituent components. Consequently, targeted modifications have been made to the outer surface of HNTs (Fig. 1), using various functionalizing agents. Fig. 3 showcases the

scanning electron microscopy (SEM) images of both pre and post-functionalized HNTs. The HNTs exhibit a cylindrical tube or rod structure having a specific surface area of 64 m^2 g^{-1}, typically measuring between 1.0 to 3 μm in length, and a diameter ranging from 30–70 nm. Numerous sorption sites are available on HNTs, making these tubes suitable for extracting heavy metals. Notably, the tube-like structure of HNTs remains consistent both before and after undergoing the functionalization process. However, the tubes appeared more rough and aggregated forming clumps after the surface functionalization in case of all modified HNTs, from H1 to H4. This change in morphology underscores the successful enhancements made to the exterior of the halloysite nanotubes that could facilitate an easy approach and attachment of heavy metal ions onto the surface of the nanotubes.

To determine the elemental makeup of the pristine and modified HNTs, energy dispersive X-ray spectroscopy (EDX) was conducted.[81] The resulting EDX spectra for both pristine HNTs (H) and modified HNTs (H1–H4) are presented in Fig. 4. Halloysite is made up of naturally formed nanotubes of aluminosilicate, predominantly consisting of the elements O, Al, and Si. The spectrum for the pure HNTs displayed peaks associated with aluminum, silicon, and oxygen, however, EDX spectra of all the functionalized HNTs displayed signals of carbon and nitrogen in addition to oxygen, aluminum and silicon, signifying the successful surface functionalization of the halloysite nanotubes.

3.3. Adsorption studies

Functionalized halloysite nanotubes (f-HNTs) that feature terminal functional groups on their external surface are highly capable of acting as chelation points for Cr(vi) ions, facilitating the removal of these metal ions from industrial wastewater and effluents. Adsorption results were further evaluated using Langmuir and Freundlich models. To attain the best adsorption results, specific variables such as contact duration, pH levels, and concentration of the adsorbate were fine-tuned while maintaining a steady adsorbent amount at 298 K. In each trial, a 10 mg dose of the adsorbent which had been previously
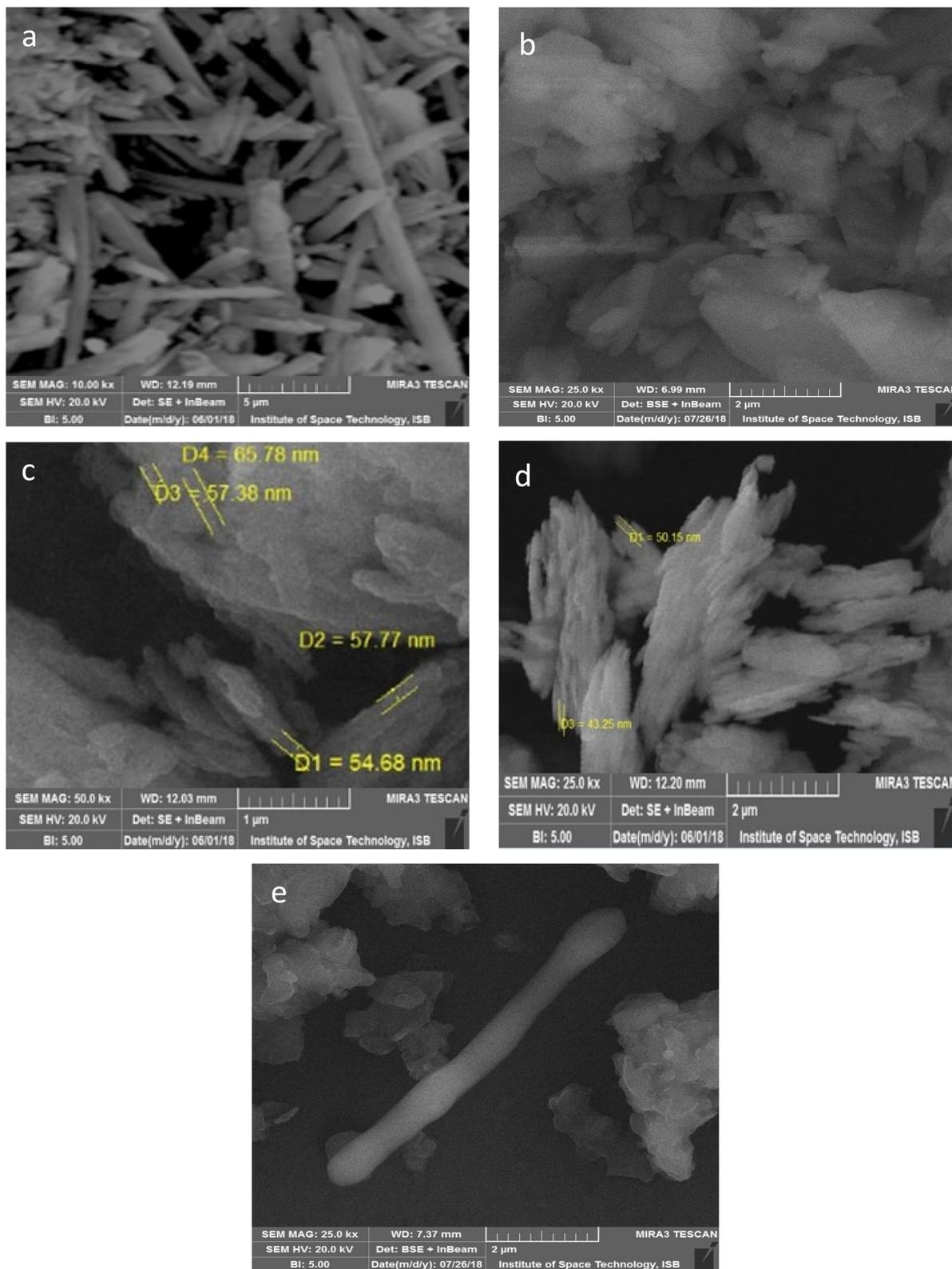
Fig. 3 SEM micrographs of (a) pristine HNTs (H) and (b–e) f-HNTs (H1–H4) samples.

determined as optimal across a varying range of a single parameter for maximum adsorption capacity was employed. This method was systematically applied to all the other parameters in turn. The mean values reported are based on three runs for each optimized parameter, with a standard deviation of ±0.01.
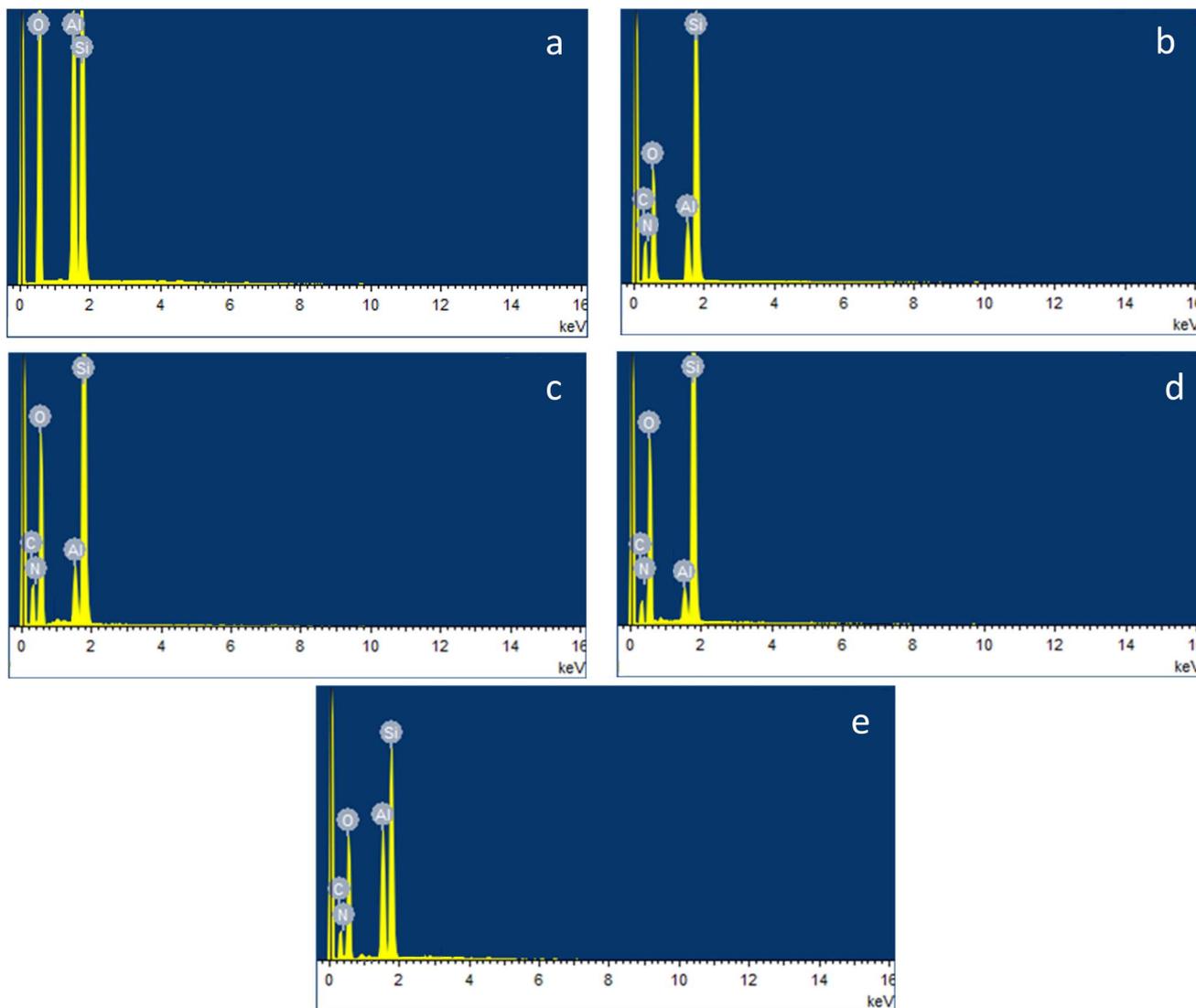
Fig. 4 EDX spectra of (a) pristine HNTs (H) and (b–e) f-HNTs (H1–H4) samples.

3.3.1 Contact time. The ability of f-HNTs (H1) to adsorb Cr(VI) ions was measured by introducing 10 mg of the material into a 10 mL solution containing 10 ppm of Cr(VI) ions at 298 K. After 30 minutes of contact time, an equilibrium was achieved, with the amidoxime-modified f-HNTs (H1) showing a maximum Cr(VI) ion adsorption rate of 91%, as depicted in Fig. 5. In a similar manner, the adsorption rates at equivalent contact times were also evaluated for other adsorbents, including hydrazone-modified HNTs (H2), EDA-modified HNTs (H3), and DETA-modified HNTs (H4). Fig. 5 reveals that the optimal adsorption capacities for H2, H3, and H4 to capture Cr(VI) ions were 94%, 66%, and 58% respectively, all within the 30 minute window. This notable proficiency in Cr(VI) ions adsorption by the f-HNTs can be attributed to the presence of hydroxyl and amine groups, which interact significantly with the metal ions. Initially, there was a marked uptake percentage due to the abundance of active groups receptive to Cr(VI) ions. However, as time progressed, this uptake efficiency stayed constant as the available adsorption sites became increasingly occupied.

3.3.2 pH. pH plays a pivotal role in influencing the adsorption of heavy metal ions. When investigating the impact of pH on the adsorption of Cr(VI) ions, it was observed across a pH spectrum of 2–10 at constant adsorbent dose (10 mg) with a contact time of 30 min, as illustrated in Fig. 6. The most optimal adsorption capacity was identified at a lower acidic pH of 3. Beyond this point, the adsorption remained stable for a bit and subsequently decreased. The amidoxime-modified HNTs (H1) were able to adsorb 91% of the Cr(VI) ions. In a more acidic environment with a pH ranging from 2.0 to 6.0, Cr(VI) primarily exists as hydrogen chromate ion ($HCrO_4^-$), however, when the pH exceeds 6, chromate ions (CrO_4^{2-}) becomes the dominant form. Under acidic conditions, the NH_2 groups on the surface of f-HNTs' abstract a proton from the $HCrO_4^-$ ion. This results in the creation of NH_3^+ species. Consequently, an efficient adsorption process occurs due to the electrostatic attraction between the negatively charged chromate ion and the positively charged NH_3^+ groups. As the pH increases, the ability of the amine groups to accept protons diminishes, which results in
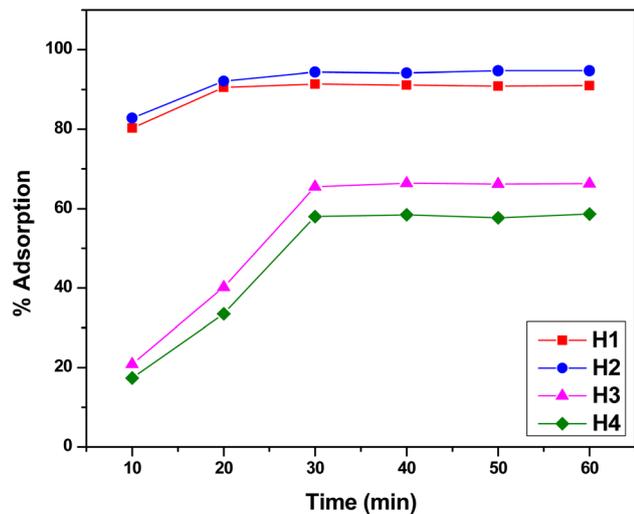
Fig. 5 Effect of contact time on the adsorption capacity of f-HNTs (H1–H4).
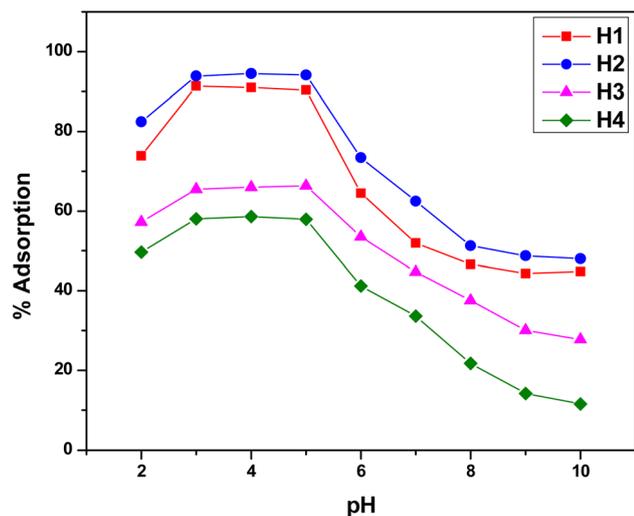

Fig. 6 Effect of pH on the adsorption capacity of f-HNTs (H1–H4).

a reduced uptake of Cr(VI) ions which subsequently reduces the adsorption efficiency. When using hydrazone-modified HNTs (H2), the adsorption efficiency peaked at 94% within 30 minutes at a pH of 3 as shown in Fig. 6. This increased adsorption efficiency can be attributed to the presence of a greater number of amino groups in H2 sample compared to H1. The adsorption efficiency of EDA-modified HNTs (H3) was found to be 66%, which is notably lower than that of H1 and H2. While the NH₂ groups of EDA are protonated similar to H1 and H2, one would expect ethylenediamine, being a bidentate molecule with a chelating nature, to display higher efficiency. However, the molecular hindrance among them potentially impairs the ability of EDA to absorb Cr(VI) ions, leading to this diminished adsorption value. On the other hand, sample H4 (DETA-modified HNTs) reveals the adsorption efficiency of 58%, which is even less than H1, H2, and H3 samples. At lower pH levels, the NH_2 groups of DETA become protonated, forming

NH_3^+, which then attracts chromate anions through electrostatic forces of attraction. Yet, since DETA acts as a tridentate ligand, it might introduce more pronounced steric hindrance between the ions, subsequently causing a substantial decrease in the adsorption efficiency, plummeting to 12% at elevated pH levels.

3.3.3 Adsorbate concentration. The adsorptive capabilities of f-NHTs were observed across a range of metal ion concentrations, spanning from 10 to 150 ppm, and conducted at a pH of 3 for 30 minutes with 10 mg of f-HNTs. Fig. 7 illustrates the impact of these metal ion concentrations on the adsorption capacity for four distinct adsorbents: H1, H2, H3, and H4. The observed trend indicated that as the concentration of metal ions rose, there was a corresponding decrease in Cr(VI) adsorption efficiency. All the nano-adsorbents reached their peak adsorption at 10 ppm; beyond this concentration, a decline in adsorption was noted. This diminishing trend could be ascribed to the reduced availability of active adsorption sites with escalating metal concentration.

3.3.4 Comparative sorption of Cr(VI) ions by f-HNTs (H1–H4). Various f-HNTs have shown promise as nano-sorbents due to the presence of oxygen and nitrogen-containing functional groups on their surface.[82,83] The adsorption efficiency of Cr(VI) ions on f-HNTs was evaluated at optimized conditions including a pH of 3, a contact duration of 30 minutes, an adsorbate concentration of 10 ppm using 10 mg of the adsorbent. The optimal adsorption rates of Cr(VI) ions on various f-HNTs ranged between 58% to 94% as depicted in Fig. 8. This adsorption range is largely influenced by the binding capacities of the various f-HNTs with the Cr(VI) ions owing to the specific functional groups intentionally introduced on the surface of HNTs. The mechanism for this adsorption involves the electrostatic interactions and chemical bonding between Cr(VI) ions and the surface groups of f-HNTs. The results reveal that the increased binding potential of f-HNTs positions them as emerging contenders in the realm of adsorbing nanomaterials.
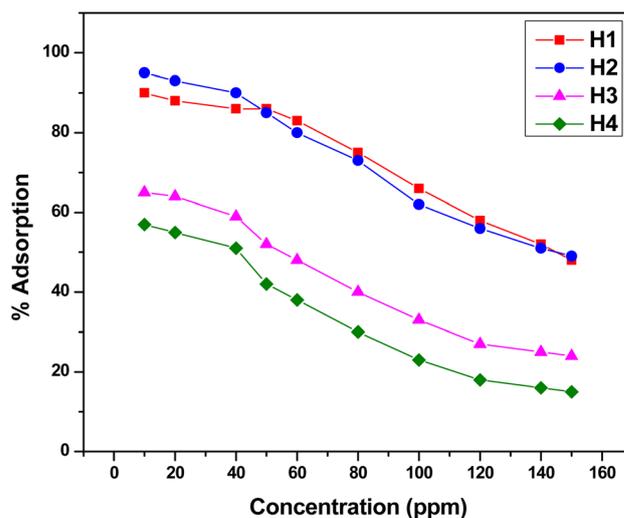

Fig. 7 Effect of adsorbate concentration on the adsorption capacity of f-HNTs (H1–H4).
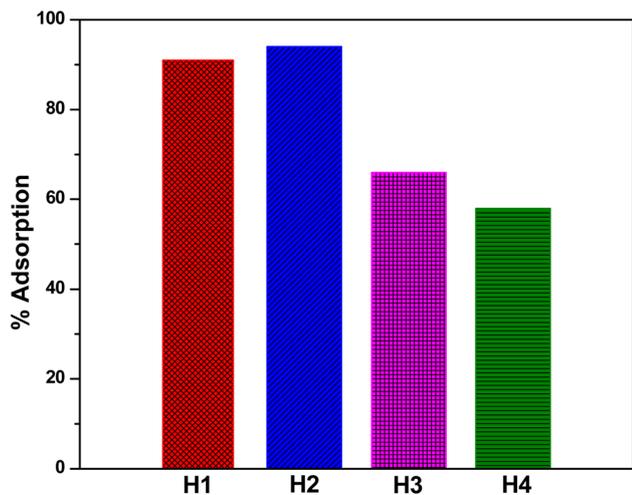
Fig. 8 Maximum uptake of Cr(VI) ions at optimized parameters by f-HNTs (H1–H4).

3.3.5 Comparison of f-HNTs with other adsorbents for Cr(VI) uptake. A comparison of Cr(VI) adsorption capacity with other previous works has been given in Table 1. The table clearly reflects that the adsorption capacity of f-HNTs is relatively higher than other modified HNTs like HDTMA-HNTs, HNT-PUS and also SWCNTs/MWCNTs. The decorated HNTs showcased outstanding performance in removing maximum Cr(VI) pollutant in terms of its shorter span of time and relatively broader range of acidic environment than others.

3.3.6 Adsorption isotherms. The adsorption process is typically assessed based on several characteristics of the adsorbent surface, including the type of functional groups it contains. Commonly recognized mechanisms of adsorption encompass electrostatic attraction, complexation, chelation, and hydrogen bonding. Under acidic conditions, the protonation of amine groups can be readily initiated, making the adsorption of the Cr(VI) anion through electrostatic interactions highly plausible. During the adsorption procedure, the solute that gets adsorbed onto the surface of the adsorbent is in a dynamic equilibrium with the solute concentration in the solution. The solute quantity adsorbed on the adsorbent surface (represented as q_e) with respect to the solute quantity at equilibrium in the solution (represented as C_e) at a constant temperature yields an adsorption isotherm, which can be elucidated using specific adsorption models. The well-known Freundlich and Langmuir adsorption models, in particular, were employed to delineate the interaction between the adsorbent and the adsorbate.[88,89] The data collected from all f-HNTs nano-sorbent systems, designed for the uptake of Cr(VI) ions, was analyzed using the appropriate isotherms to determine the most fitting trend. The information regarding f-NHTs was examined using parameters from both Freundlich and Langmuir adsorption isotherms. As a result, the Langmuir monolayer adsorption model was deemed more suitable, suggesting that f-HNTs offer homogenous donor sites. The nano-sorbents' diverse active sites effectively adsorb Cr(VI) ions from the aqueous solution. Herein, both correlation factors and equilibrium parameters were computed using Freundlich and Langmuir adsorption models, as presented in Table 2. The correlation coefficients, R^2 values, from these isotherms, indicate that the data aligns more accurately with the Langmuir model than the Freundlich model as shown in Fig. 9 and 10, revealing that Cr(VI) adsorption mainly adheres to the Langmuir isotherm. Furthermore, the oxygen and nitrogen functionalities

Table 1 Comparison of adsorption efficiency of f-HNTs with other adsorbents reported in literature

| Adsorbent | Pollutant | Adsorption parameters | | | References |
		pH	Contact time	Adsorption capacity (%)	
Halloysite nanotubes-hexadecyltrimethylammoniumbromide (HNT-HDTMA)	Cr(VI)	3	60 min	90%	63
Halloysite nanotubes-polyurethane sponge (HNT-PUS)	Cr(VI)	2–3	20–60 min	77.4%	69
Polyvinylideneflouride – halloysite nanotubes-γ-Aminopropyltriethoxysilane (PVDF – HNTs – APTES)	Cr(VI)	5.5	180 min	52.3%	84
Single walled carbon nanotubes (SWCNTs)	Cr(VI)	2.5	60 min	88%	85
Multi walled carbon nanotubes (MWCNTs)				76%	
Halloysite nanotubes-zerovalent iron (HNT-Fe0)	Cr(VI)	5	24 h	77.1%	86
H10 H25				65.7%	
2D/2DBiVO₄/MXene (BiVO₄: bismuth vanadate, MXene: transition metal carbide and nitride)	Cr(VI)	3	120 min	83.6%	87
Functionalized halloysite nanotubes (f-HNTs)	Cr(VI)	3–5	30 min	>90%	This work

Table 2 Langmuir and Freundlich isotherm parameters for the adsorption of Cr(VI) ions by f-HNTs

Sample	Metal ion	Langmuir parameters				Freundlich parameters		
		R^2	Q_o	b	R_L	R^2	K_f	n
H1	Cr(VI)	0.99555	83.195	0.12245	0.4495	0.87353	13.187	2.238
H2	Cr(VI)	0.99239	64.977	0.3158	0.2405	0.92666	16.215	2.633
H3	Cr(VI)	0.98942	46.404	0.0480	0.6754	0.858	5.303	2.293
H4	Cr(VI)	0.96799	30.618	0.0555	0.643	0.70891	5.019	2.828

on the f-HNTs surfaces are widely recognized as efficient metal adsorption sites. Hence, f-HNTs offer ample active sites to bind with Cr(VI) entities through coordination or electrostatic interactions. Both models showed a linear trend, indicating the suitability of these isotherms for the adsorption process. Essential elements of the Langmuir parameter can be utilized to assess the affinity between the adsorbate and the adsorbent. This relationship can be described using a dimensionless constant known as the separation factor or equilibrium parameter (R_L).

The R_L value displays characteristics of a Langmuir isotherm: it is irreversible when R_L equals 0, linear at R_L equals 1, unfavorable when R_L is greater than 1, and favorable when R_L is between 0 and 1. Specifically, R_L values between 0 and 1 indicate favorable adsorption conditions. Table 1 suggests that the adsorption process is advantageous, as the R_L value was observed to be within the 0.24–0.67 range. This implies that the binding of Cr(VI) ions to f-HNTs is favorable. Furthermore, the data indicates the monolayer adsorption of Cr(VI) ions by f-HNTs, adhering to the Langmuir isotherm model.
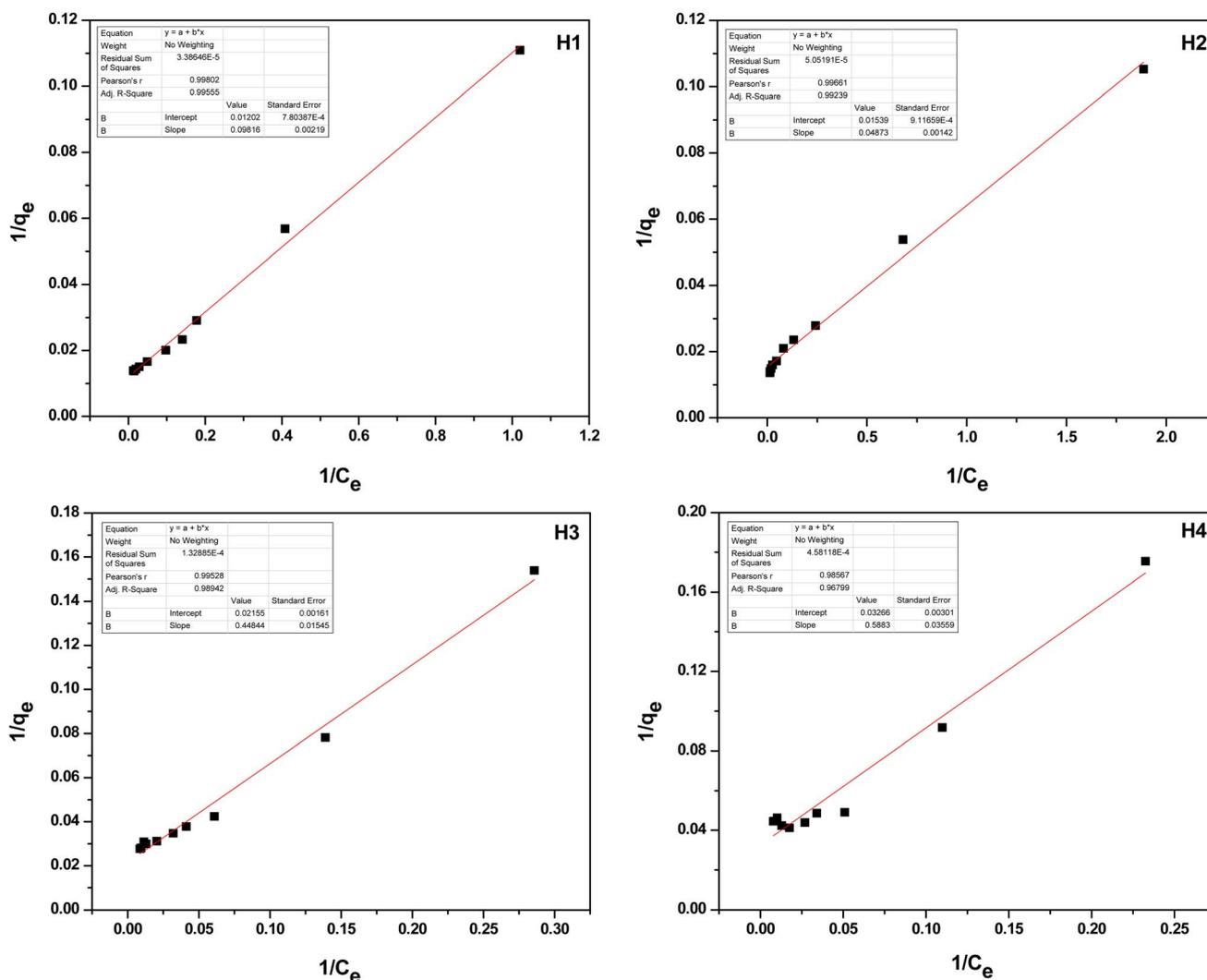

Fig. 9 Langmuir adsorption isotherms for various f-HNTs (H1–H4).

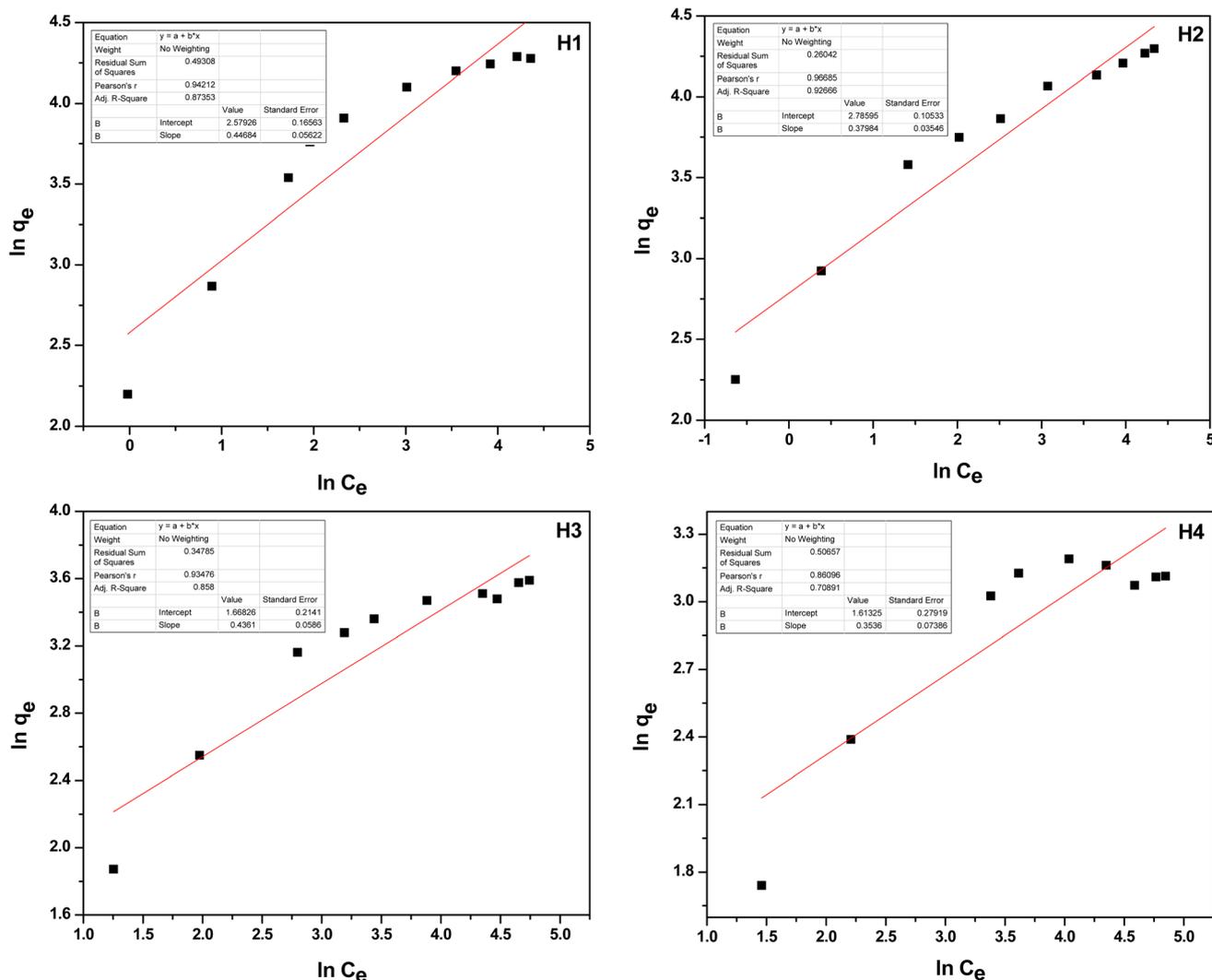© 2024 The Author(s). Published by the Royal Society of Chemistry

Fig. 10 Freundlich adsorption isotherms for various f-HNTs (H1–H4).

Consequently, it can be inferred that there are homogenous active sites available for Cr(VI) ions uptake.

3.4. Computational analysis

To corroborate the findings from the experiments, theoretical analyses employing quantum chemistry's computational techniques have been conducted. Specifically, calculations using density functional theory (DFT) were executed to grasp the molecular–level interactions occurring between the four types of functionalized halloysite nanotubes and the $HCrO_4^-$ anion. The models H1 and H2 of halloysite are distinguished solely based on the C=N–R group variations. In the case of H1, the R component is equated to OH, forming an oxime, whereas for H2, R takes the form of NH_2, resulting in a hydrazone. This distinction is crucial for comprehending their divergent interactions with $HCrO_4^-$. H2 demonstrates a more pronounced affinity for this particular anion, as evidenced by a significantly higher interaction energy value, specifically, -26.33 kcal mol^{-1}, in stark contrast to H1's -20.56 kcal mol^{-1}, as illustrated in Fig. 11. This phenomenon can be attributed to the formation of
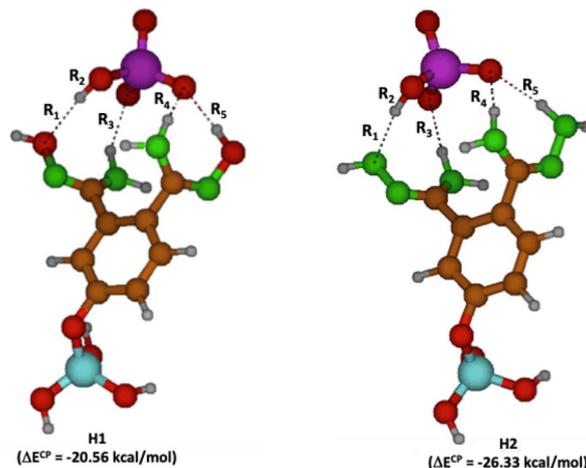

Fig. 11 Molecular models for H1–$HCrO_4^-$ (left) and H2–$HCrO_4^-$ (right) complexes. Oxygen atoms in red, nitrogen in green, carbon in brown, chromium in purple, hydrogen in grey and silicon in aqua.
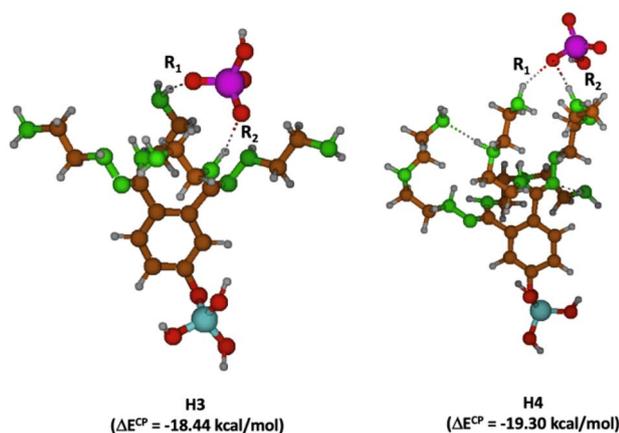
Table 3 Selected bond distances (R_i), in Å, for complexes of $HCrO_4^-$ with H1 and H2 models

f-HNTs	R_1	R_2	R_3	R_4	R_5
H1	1.975	0.970	2.005	2.031	1.793
H2	1.919	0.980	1.860	2.018	2.029

comparatively stronger hydrogen bonds with the NH functionalities of the hydrazone, as opposed to the weaker bonds formed by the OH groups in the oxime. The strength of these bonds is manifest in the altered atomic distances within the hydrogen bonds. In Fig. 11, the complexes of $HCrO_4^-$ with H1 and H2 are illustrated, and the bond distances are prominently marked as R_i (where i ranges from 1 to 5). Across both complexes, a total of four hydrogen bonds are formed, yet the bond lengths tend to be notably shorter in the complex involving H2, suggesting a more robust interaction (Table 3).

On the other hand, R_2 represents the distance of the O–H bond within the $HCrO_4^-$ anion. A lengthier R_2 denotes a more pronounced transfer of the acidic proton toward the HNTs, which also implies a more intense interaction.

The H3 and H4 variants are distinguished by the differing lengths of the chains that are attached to the hydrazone moiety. Examining the interactions within these molecular structures, it becomes apparent that the extended chain lengths in both cases act as a barrier to the establishment of hydrogen bonds with $HCrO_4^-$, owing to the relative disposition and presence of intramolecular hydrogen bonds among chains. Fig. 12 demonstrates that in both scenarios, merely two hydrogen bonds are formed.

Fig. 12 Molecular models for H3–$HCrO_4^-$ (left) and H4–$HCrO_4^-$ (right) complexes. Oxygen atoms in red, nitrogen in green, carbon in brown, chromium in purple, hydrogen in grey and silicon in aqua.

Table 4 Selected bond distances (R_i), in Å, for complexes of $HCrO_4^-$ with H3 and H4 models

f-HNTs	R_1	R_2
H3	2.001	2.037
H4	2.217	2.176

Additionally, it is worth noting that the OH group in $HCrO_4^-$ plays no role in these interactions. Consequently, the interaction energies for H3 and H4 are lower, registering at −18.44 and −19.30 kcal mol^{-1} respectively compared to H1 and H2, a finding that is consistent with experimental data (Table 4). However, despite these results, H4 exhibits a marginally higher (by less than 1 kcal mol^{-1}) interaction energy compared to H3. Contrarily, experimental observations indicate that H3 has a superior ability to bind with $HCrO_4^-$. This discrepancy could potentially be attributed to the inherent limitations of the simplified molecular model being employed, suggesting that a more accurate representation of the interactions with $HCrO_4^-$ might necessitate accounting for the additional chains.

4. Conclusions

The functionalization of pristine halloysite nanotubes was successfully achieved through the incorporation of various entities, resulting in the creation of four distinct types of functionalized halloysite nanotubes (f-HNTs). Techniques such as FTIR, XRD, SEM and EDX were employed to characterize the f-HNTs, confirming that the functionalization was successfully implemented on their external surfaces. The conducted adsorption studies demonstrated a significant dependence of Cr(vi) ions adsorption by the f-HNTs on factors including pH level, duration of contact, and the concentration of Cr(vi) ions. When applied for the adsorption of Cr(vi) ions, the functionalized HNTs showcased an outstanding performance, capturing over 90% within a mere 30 minutes at a pH level of 3 for H1 and H2, while H3 and H4 achieved 66% and 58% adsorption, respectively. The Langmuir adsorption isotherm model indicated a favorable adsorption process, with the R_L value ranging between 0 and 1. The f-HNTs featured hydroxyl and amine groups, and the interactions between the Cr(vi) ions and the adsorbents were primarily electrostatic. Further investigation through quantum chemical calculations disclosed that halloysite nanotubes adorned with hydrazone formations (H2) exhibited a stronger propensity (interaction energy −26.33 kcal mol^{-1}) toward Cr(vi) ions. This phenomenon can be attributed to the generation of more robust hydrogen bonds with the NH components of the hydrazone segment, surpassing the bonds formed by the OH group in oxime (H1) and the extended amine chains seen in H3 and H4. Based on these findings, the decorated HNTs present themselves as economically advantageous adsorbents for potential applications in removing Cr(vi) from polluted water. In future studies, we will further investigate the performance of these decorated HNTs on real wastewater samples to expand their applications.

Conflicts of interest

There are no conflicts to declare.

Acknowledgements

at Quaid-i-Azam University. Prof. Dr Sonia Zulfiqar is highly thankful for the support provided by the Statutory City of Ostrava, Czechia through Research Grant "Global Experts".

References

1 P. K. Rai, *Int. J. Phytorem.*, 2008, **10**, 133–160.

2 L. Järup, *Br. Med. Bull.*, 2003, **68**, 167–182.

3 O. B. Akpor, G. O. Ohiobor and T. D. Olaolu, *Adv. Biosci. Bioeng.*, 2014, **2**, 37–43.

4 J. Takala, *Introductory Report: Decent Work–Safe Work*, XVIth World Congress on Safety and Health at Work, 2002.

5 Z. L. He, X. E. Yang and P. J. Stoffella, *J. Trace Elem. Med. Biol.*, 2005, **19**, 125–140.

6 J. O. Duruibe, M. Ogwuegbu and J. Egwurugwu, *Int. J. Phys. Sci.*, 2007, **2**, 112–118.

7 D. Lide, *Handbook of Chemistry and Physics*, CRC Press Inc., Boca Raton, FL, 73rd edn, 1992.

8 C. H. Yun, R. Prasad, A. K. Guha and K. K. Sirkar, *Ind. Eng. Chem. Res.*, 1993, **32**, 1186–1195.

9 R. M. Sedman, J. Beaumont, T. A. McDonald, S. Reynolds, G. Krowech and R. Howd, *J. Environ. Sci. Health, Part C: Environ. Carcinog. Ecotoxicol. Rev.*, 2006, **24**, 155–182.

10 M. Owlad, M. K. Aroua, W. A. W. Daud and S. Baroutian, *Water, Air, Soil Pollut.*, 2009, **200**, 59–77.

11 C. V. Mohod and J. Dhote, *Int. J. Innov. Res. Technol. Sci. Eng.*, 2013, **2**, 2992–2996.

12 T. W. Clarkson, *Environ. Health Perspect.*, 1993, **100**, 31.

13 A. Sigel and H. Sigel, *Metal Ions in Biological Systems: Volume 34: Mercury and its Effects on Environment and Biology*, CRC Press, 1997.

14 J. Roberts, *Meat Toxicity in Children. Training Manual Pediatric Environmental Health: Putting It Into Practice*, Emeryville, CA, 1999.

15 M. Costa, *Toxicol. Appl. Pharmacol.*, 2003, **188**, 1–5.

16 E. Vunain, A. Mishra and B. Mamba, *Int. J. Biol. Macromol.*, 2016, **86**, 570–586.

17 W. H. Organization, *Guidelines for the Safe Use of Wastewater, Excreta and Greywater*, World Health Organization, 2006.

18 H. Polat and D. Erdogan, *J. Hazard. Mater.*, 2007, **148**, 267–273.

19 X.-j. Hu, J.-s. Wang, Y.-g. Liu, X. Li, G.-m. Zeng and Z.-l. Bao, *J. Hazard. Mater.*, 2011, **185**, 306–314.

20 S. Pal, A. S. Patra, S. Ghorai, A. K. Sarkar, R. Das and S. Sarkar, *Environ. Sci.: Water Res. Technol.*, 2015, **1**, 84–95.

21 C. Y. Teh, P. M. Budiman, K. P. Y. Shak and T. Y. Wu, *Ind. Eng. Chem. Res.*, 2016, **55**, 4363–4389.

22 M. Razali, J. F. Kim, M. Attfield, P. M. Budd, E. Drioli and Y. M. Lee, *Green Chem.*, 2015, **17**, 5196–5205.

23 M. Min, L. Shen, G. Hong, M. Zhu, Y. Zhang and X. Wang, *Chem. Eng. J.*, 2012, **197**, 88–100.

24 G. I. Fakhrullina, F. S. Akhatova, Y. M. Lvov and R. F. Fakhrullin, *Environ. Sci.: Nano*, 2015, **2**, 54–59.

25 A. Kongsuwan, P. Patnukao and P. Pavasant, *J. Ind. Eng. Chem.*, 2009, **15**, 465–470.

26 M. Guo, G. Qiu and W. Song, *Waste Manage.*, 2010, **30**, 308–315.

27 M. A. Tofighy and T. Mohammadi, *J. Hazard. Mater.*, 2011, **185**, 140–147.

28 K. Pillay, E. Cukrowska and N. Coville, *J. Hazard. Mater.*, 2009, **166**, 1067–1075.

29 G. P. Rao, C. Lu and F. Su, *Sep. Purif. Technol.*, 2007, **58**, 224–231.

30 M. Betancur, P. Bonelli, J. Velásquez and A. Cukierman, *Bioresour. Technol.*, 2009, **100**, 1130–1137.

31 G. Sheng, S. Wang, J. Hu, Y. Lu, J. Li and Y. Dong, *Colloids Surf., A*, 2009, **339**, 159–166.

32 A. Lu, S. Zhong, J. Chen, J. Shi, J. Tang and X. Lu, *Environ. Sci. Technol.*, 2006, **40**, 3064–3069.

33 D. Mohan and S. Chander, *J. Hazard. Mater.*, 2006, **137**, 1545–1553.

34 S. J. Köhler, P. Cubillas, J. D. Rodríguez-Blanco, C. Bauer and M. Prieto, *Environ. Sci. Technol.*, 2007, **41**, 112–118.

35 R. Apiratikul and P. Pavasant, *Chem. Eng. J.*, 2008, **144**, 245–258.

36 S. A. Al-Jlil and F. D. Alsewailem, *Appl. Clay Sci.*, 2009, **42**, 671–674.

37 X. Gu and L. J. Evans, *Geochim. Cosmochim. Acta*, 2008, **72**, 267–276.

38 Z.-R. Liu, L.-M. Zhou, W. Peng, Z. Kai, C.-X. Wen and H.-H. Lan, *J. China Univ. Min. Technol.*, 2008, **18**, 255–260.

39 K. G. Bhattacharyya and S. S. Gupta, *Appl. Clay Sci.*, 2008, **41**, 1–9.

40 F. Shahamati Fard, S. Akbari, E. Pajootan and M. Arami, *Desalin. Water Treat.*, 2016, **57**, 26222–26239.

41 J. Duan, R. Liu, T. Chen, B. Zhang and J. Liu, *Desalination*, 2012, **293**, 46–52.

42 K. Zhu, Y. Duan, F. Wang, P. Gao, H. Jia and C. Ma, *Chem. Eng. J.*, 2017, **311**, 236–246.

43 R. Li, Z. Hu, S. Zhang, Z. Li and X. Chang, *Int. J. Environ. Anal. Chem.*, 2013, **93**, 767–779.

44 Q. He, D. Yang, X. Deng, Q. Wu, R. Li and Y. Zhai, *Water Res.*, 2013, **47**, 3976–3983.

45 R. Li, Q. He, Z. Hu, S. Zhang, L. Zhang and X. Chang, *Anal. Chim. Acta*, 2012, **713**, 136–144.

46 A. A. Maamoun, A. Elkhateeb and S. Zulfiqar, *Ind. Eng. Chem. Res.*, 2022, **61**, 17937–17949.

47 M. Zhang, Y. Wang, Y. Zhang, L. Ding, J. Zheng and J. Xu, *Appl. Surf. Sci.*, 2016, **375**, 154–161.

48 Y. Zhang, M. Zhang, J. Yang, L. Ding, J. Zheng and J. Xu, *J. Alloys Compd.*, 2017, **695**, 3256–3266.

49 M. Zhang, Y. Ling, L. Liu, J. Xu, J. Li and Q. Fang, *Inorg. Chem. Front.*, 2020, **7**, 3081–3091.

50 S. Xie, Y. Xiao, N. Lu and M. Zhang, *CrystEngComm*, 2023, **25**, 4427–4434.

51 X. Guo, Y. Xie, B. Zhang, J. Xu, L. Yan and M. Zhang, *Colloids Surf., A*, 2022, **636**, 128167.

52 R. Baby, B. Saifullah and M. Z. Hussein, *Nanoscale Res. Lett.*, 2019, **14**, 341.

53 M. Liu, Z. Jia, D. Jia and C. Zhou, *Prog. Polym. Sci.*, 2014, **39**, 1498–1525.

54 P. Yuan, D. Tan and F. Annabi-Bergaya, *Appl. Clay Sci.*, 2015, **112**, 75–93.

55 S. Jana, S. Das, C. Ghosh, A. Maity and M. Pradhan, *Sci. Rep.*, 2015, **5**, 8711.

56 S. Zulfiqar, F. Karadas, J. Park, E. Deniz, G. D. Stucky and Y. Jung, *Energy Environ. Sci.*, 2011, **4**, 4528–4531.

57 Y. Yang, Y. Chen, F. Leng, L. Huang, Z. Wang and W. Tian, *Appl. Sci.*, 2017, **7**, 1215.

58 E. Abdullayev and Y. Lvov, *Dev. Clay Sci.*, 2016, **7**, 554–605.

59 Y. Zhao, E. Abdullayev, A. Vasiliev and Y. Lvov, *J. Colloid Interface Sci.*, 2013, **406**, 121–129.

60 M. Zhao and P. Liu, *Microporous Mesoporous Mater.*, 2008, **112**, 419–424.

61 P. Yuan, P. D. Southon, Z. Liu, M. E. Green, J. M. Hook and S. J. Antill, *J. Phys. Chem. C*, 2008, **112**, 15742–15751.

62 X. Tian, W. Wang, Y. Wang, S. Komarneni and C. Yang, *Microporous Mesoporous Mater.*, 2015, **207**, 46–52.

63 W. Jinhua, Z. Xiang, Z. Bing, Z. Yafei, Z. Rui and L. Jindun, *Desalination*, 2010, **259**, 22–28.

64 P. Luo, J.-s. Zhang, B. Zhang, J.-h. Wang, Y.-f. Zhao and J.-d. Liu, *Ind. Eng. Chem. Res.*, 2011, **50**, 10246–10252.

65 N. Ballav, H. J. Choi, S. B. Mishra and A. Maity, *Appl. Clay Sci.*, 2014, **102**, 60–70.

66 J. Matusik and A. Wścisło, *Appl. Clay Sci.*, 2014, **100**, 50–59.

67 M. Krawczyk, S. Akbari, M. Jeszka-Skowron, E. Pajootan and F. S. Fard, *J. Anal. At. Spectrom.*, 2016, **31**, 1505–1514.

68 Z. He, Y. Li, G. Liu, C. Wang, S. Chang, J. Hu, X. Zhang and Y. Vasseghian, *Ind. Crops Prod.*, 2023, **202**, 117082.

69 K. Nie, N. Ji, J. Xu, M. Guo, Y. Wang and X. Xu, *J. Environ. Chem. Eng.*, 2022, **10**, 108308.

70 M. Zhang, H. Yu and B. Chen, *Can. J. Chem.*, 2019, **97**, 259–266.

71 N. Q. Nguyen, Y. Jeong, L. Abelmann, J. Ryu and D. Sohn, *Colloids Surf., A*, 2023, **680**, 132631.

72 S.-i. Kusakari, K. Ishidu, Y. Kimura and K. Yamada, *Trans. Mater. Res. Soc. Jpn.*, 2019, **44**, 171–176.

73 C. K. Na, H. J. Park and B. G. Kim, *J. Appl. Polym. Sci.*, 2012, **125**, 776–785.

74 Gaussian 16, Revision C. 01, M. J. Frisch, G. W. Trucks, H. B. Schlegel, G. E. Scuseria, M. A. Robb, J. R. Cheeseman, G. Scalmani, V. Barone, G. A. Petersson, H. Nakatsuji, X. Li, M. Caricato, A. V. Marenich, J. Bloino, B. G. Janesko, R. Gomperts, B. Mennucci, H. P. Hratchian, J. V. Ortiz, A. F. Izmaylov, J. L. Sonnenberg, D. Williams-Young, F. Ding, F. Lipparini, F. Egidi, J. Goings, B. Peng, A. Petrone, T. Henderson, D. Ranasinghe, V. G. Zakrzewski, J. Gao, N. Rega, G. Zheng, W. Liang, M. Hada, M. Ehara, K. Toyota, R. Fukuda, J. Hasegawa, M. Ishida, T. Nakajima, Y. Honda, O. Kitao, H. Nakai, T. Vreven, K. Throssell, J. A. Montgomery Jr, J. E. Peralta, F. Ogliaro, M. J. Bearpark, J. J. Heyd, E. N. Brothers, K. N. Kudin, V. N. Staroverov, T. A. Keith, R. Kobayashi, J. Normand, K. Raghavachari, A. P. Rendell, J. C. Burant, S. S. Iyengar, J. Tomasi, M. Cossi, J. M. Millam, M. Klene, C. Adamo, R. Cammi, J. W. Ochterski, R. L. Martin, K. Morokuma, O. Farkas, J. B. Foresman and D. J. Fox, Gaussian, Inc., Wallingford CT, 2016.

75 J.-D. Chai and M. Head-Gordon, *Phys. Chem. Chem. Phys.*, 2008, **10**, 6615–6620.

76 B. J. Lynch and D. G. Truhlar, *J. Phys. Chem. A*, 2001, **105**, 2936–2941.

77 M. Bursch, J. Mewes, A. Hansen and S. Grimme, *Angew. Chem., Int. Ed.*, 2022, **61**, e202205735.

78 S. F. Boys and F. Bernardi, *Mol. Phys.*, 1970, **19**, 553–566.

79 S. Simon, M. Duran and J. J. Dannenberg, *J. Chem. Phys.*, 1996, **105**, 11024–11031.

80 P. Zaumseil, *Semicond. Semimetals*, 1997, **45**, 261–282.

81 K. Kanda, *US Pat.*, US5065020A, 1991.

82 Z. N. Garba, A. Haruna, A. Tanimu, B. Z. Bello and Z. U. Zango, *Korean J. Chem. Eng.*, 2023, **40**, 1247–1267.

83 A. Grylewicz and S. Mozia, *Sep. Purif. Technol.*, 2021, **256**, 117827.

84 G. Zeng, Y. He, Y. Zhan, L. Zhang, Y. Pan, C. Zhang and Z. Yu, *J. Hazard. Mater.*, 2016, **317**, 60–72.

85 M. H. Dehghani, M. M. Taher, A. K. Bajpai, B. Heibati, I. Tyagi, M. Asif, S. Agarwal and V. K. Gupta, *Chem. Eng. J.*, 2015, **279**, 344–352.

86 P. Maziarz, J. Matusik and A. Radziszewska, *J. Environ. Chem. Eng.*, 2019, **7**, 103507.

87 P. Liu, J. Yi, R. Bao and H. Zhao, *ChemCatChem*, 2021, **13**, 3046–3053.

88 M. Zahra, S. Zulfiqar, W. G. Skene and M. I. Sarwar, *Polym. Int.*, 2020, **69**, 50–60.

89 M. Zahra, S. Zulfiqar, W. G. Skene and M. I. Sarwar, *Ind. Eng. Chem. Res.*, 2018, **57**, 15243–15253.